

# Speckle Photometry and Spectral Types of Close Binary Star Components

*Rick Wasson  
Orange County Astronomers  
Murrieta, California  
ricksshobs@verizon.net*

*Russell Genet  
California Polytechnic State University  
San Luis Obispo, California  
russmgenet@aol.com*

*Dave Rowe  
PlaneWave Instruments  
Adrian, Michigan  
drowesmi@aol.com*

---

## Abstract

A speckle photometry method for observation of close binary stars is described which simultaneously measures orbital positions, derives color indexes, and estimates spectral types of the individual stellar components. The method combines the techniques of speckle interferometry for diffraction-limited astrometry, bispectrum analysis for relative flux distribution of the two components, and an adaptation of differential photometry for photometric calibration. Observations in multiple Sloan filter bands yield color indexes which are correlated with spectral type. It is hoped that this method will provide complimentary information to improve the quality of stellar mass estimates in binary orbit solutions as well as estimates of spectral types. The method was assessed via speckle observations made remotely with the Fairborn Institute Robotic Observatory's 11-inch telescope through Sloan g' r' i' z' filters. Results for four binaries are presented. Spectral types, estimated by the speckle photometry method, were compared with WDS Catalog types. Standard Sloan magnitudes, color indexes and spectral types of the individual binary components are provided and discussed, as well as the within-night and night-to-night variations and error sources. Finally, suggestions are provided on how this method might be refined and further validated.

---

## 1. Introduction

Stellar masses are one of the fundamental building blocks of Astronomy. Binary star systems are important because not only can the masses of the component stars can be determined from accurately measured orbits, but other stellar parameters can also be derived. Measurement of color indexes and corresponding spectral types of the individual components can provide useful supplementary information to support binary orbit solutions and more accurate definition of stellar masses and other properties for both the individual components and the total binary system (McAlister, 1985, Horch, et al, 2001, 2004 and 2006).

Speckle interferometry and Bispectrum (triple correlation) analysis to measure orbits have become standard techniques used by professional astronomers for astrometric observation of binary stars to determine stellar masses and ages (Davidson et al., 2009). Other types of observations—spectroscopy, photometry, and polarimetry—help constrain stellar properties, but are challenging to obtain for close binaries having short orbital periods.

Binary stars are often resolved as separate stars, i.e., visual binaries. But many visual binaries have long orbital periods which are poorly known. Identification of spectral types of the components may help estimate orbits and masses before a complete orbit has been observed. Close binaries with rapid motion may be detected by spectroscopy (spectroscopic binaries), but many of these are not resolvable even with large apertures. Binaries which overlap both the astrometric and spectroscopic domains can have accurate, well constrained orbits and masses, but such systems are rare.

Most close visual binaries have not been resolved spectroscopically because they are too close, one component is faint, or there is inadequate telescope time with sufficient resolution. The method described here may be applied to many known or suspected binaries. The method uses speckle interferometry for astrometry, bispectrum analysis for flux proportions, and multi-band observations of color index for spectral types of the individual binary components.

The speckle photometry method for observation of close binary stars presented here simultaneously measures the apparent orbital position, the proportion of flux from each component star, and their standard Sloan magnitudes. Observations in multiple filters yields calibrated color indexes for each binary component, which are then used to estimate the spectral type of the individual stars.

The method combines the techniques of speckle interferometry, for diffraction-limited resolution, with a modified version of differential photometry for photometric self-calibration. Speckle bispectrum analysis yields both astrometry and flux measurements. The two binary component stars are referred to below as A (primary) and B (secondary).

The speckle photometry method has eight major observation and data reduction steps which are summarized here and discussed in detail with example data below:

1. Normal speckle observations
2. Flux proportions
3. Long exposures
4. Photometric self-calibration
5. Component standard magnitudes
6. Component color indexes
7. Reference star
8. Component spectral types

Over the last decade, one of us (DR) has developed free Windows-based software packages that enable amateurs and students to join in speckle interferometric observations of double stars. These programs make it easy to find appropriate targets in the Washington Double Star Catalog (WDS) (Rowe 2017) and in the Gaia DR2 database (Rowe, 2018); perform speckle autocorrelation analysis (Rowe, & Genet, 2015) and (Harshaw, Rowe & Genet, 2017); and explore bispectrum analysis (Rowe, 2020). In 2020, one of us (RG) completed building a remotely accessible observatory for speckle observations by students and amateur mentors. Several teams have already made observations and published papers (Marchetti et al., 2020), Caputo et al., 2020, Altunin et al., 2020), Marchetti, et al., 2021). More papers are in publication.

To explore the potential of this method, the WDS Catalog was searched, using the WDS1.2 program (Rowe, 2017) with the following search limits:  $0.7'' < \rho < 3''$ ;  $M_A < 10$ ;  $\text{Dec} > 0$ ; and  $\Delta\text{magnitude} < 2$ . The resulting long lists were then scanned manually to find stars that have *estimated orbits* (WDS note "O") and known spectral types for *both* components. Orbit details were then taken from the 6<sup>th</sup> Orbit Catalog. It was a surprise to find that relatively few binaries in the Washington Double Star (WDS) Catalog (only a few percent) have spectral types given for both components.

The binaries in Table 1 were chosen for initial validation observations because they were easily accessible during fall and winter evenings, covered a range of separation within the seeing disk, and the components of these systems sampled a broad range of WDS spectral types, A F G K M. It is noted that the Hipparcos and Gaia satellites have already resolved these binaries and provided high-quality photometry for them. However, once validated with a small telescope, this method should enable speckle photometry with larger apertures that could reach smaller separations (and hence shorter periods), well below the  $\sim 0.6''$  Gaia resolution limit.

Table 1. Summary of characteristics of the four binary stars observed in this initial development of the Speckle Photometry method. The first 6 columns are from the WDS Catalog: WDS coordinates, Discovery code, magnitude (assumed to be V band), predicted  $\theta$  and  $\rho$  on 2021.0 (from the 6<sup>th</sup> Orbit Catalog), WDS spectral type, and orbital period (6<sup>th</sup> Orbit Catalog). Supplementary data from the Gaia (DR2) catalog is also provided: Gaia G magnitude, (Bp-Rp) color index, parallax (milli-arc-seconds), and distance (parsecs).

WDS Data for Binary Stars Observed						Gaia Data			
Coordinates	Discovery	Mag (V)	Ephemerides	Spec Type	Orbit Period	G	Bp-Rp	Parallax	Distance
		A	$\theta$ (deg)	A	(yr)	A	A	(mas)	(pcs)
		B	$\rho$ (")	B		B	B		
22280+5742	KR 60AB	9.93	205.5	M3.5	44.58	8.641	2.692	249.68	4.01
		11.41	2.057	M4.5		9.911	2.914		
23050+3322	STF 2974AB	8.07	166*	A0V	None	8.044	0.061	4.07	245.7
		8.46	2.7*	A3V		8.384	0.251		
00014+3937	HLD 60	9.09	165.1	K0V	217.3	8.872	0.983	19.47	51.4
		9.77	1.329	K1V		9.395	1.196		
04301+1538	STF 554	5.7	15.1	F0V	172.5	5.591	0.413	21.03	47.6
		8.12	1.43	G0V		7.869	1.226		

\* No orbit has been estimated for this long-period system. The values are the last reported in WDS (2016).

The three goals of this project were to:

- Explore the capabilities of speckle photometry to measure the component magnitudes in several standard photometric bands.
- Demonstrate whether color indexes of the individual components could be measured with sufficient accuracy to estimate their spectral types.
- Evaluate the uncertainties inherent in the method and identify the major sources of uncertainty.

## 2. Equipment

Observations were made with the Fairborn Institute Remote Observatory (FIRO) telescope shown in Figure 1 (Marchetti, Caputo, and Genet, 2020). The telescope consists of C-11 optics on a custom “L” mount driven by a SiTech Control system (Gray, 2020). Instrumentation consists of a ZWO ASI 1600MM CMOS camera, 1.5X Barlow lens, automated Clement focuser, and five-position filter wheel with Sloan filters: g', r', i', and z' (Generation 2 filters from Astrodon).



Figure 1. The Fairborn Institute’s robotic observatory (FIRO) was accessed remotely in real time for the observations described in this paper.

The Astrodon filter characteristics, shown in Figure 2, were designed to match wavelengths of the Sloan Digital Sky Survey (SDSS) as closely as possible, but have higher transmission (up to 99%). The front-illuminated CMOS camera quantum efficiency (QE) declines earlier than the back-illuminated CCD detectors used in SDSS. Therefore, the Astrodon z'2 long-pass filter was chosen to maximize sensitivity. After these observations were made, the ZWO ASI 1600 camera was replaced with a ZWO ASI 183 camera which has a backside illuminated chip with higher QE out in the red.

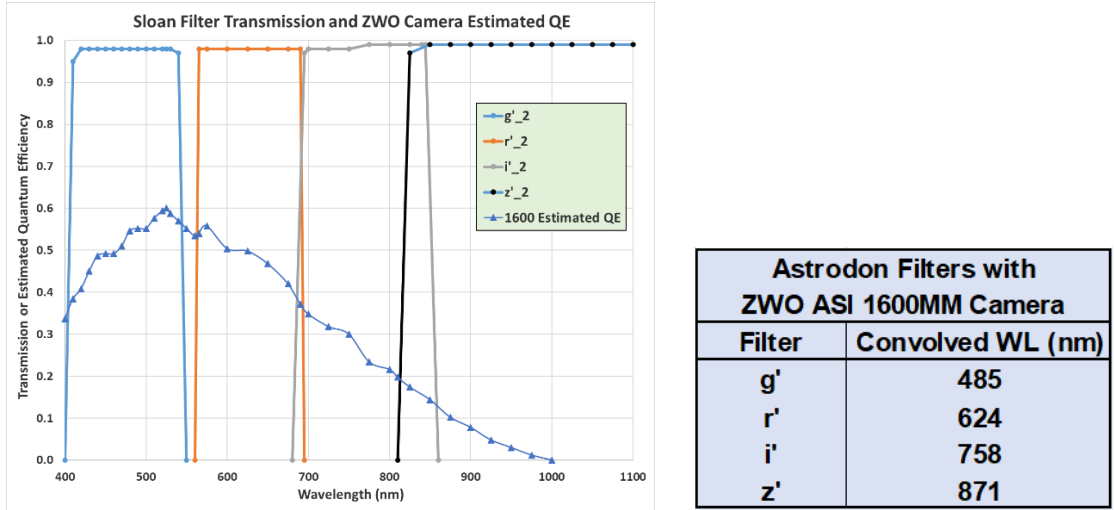


Figure 2. Left: The Astrodon filter set was used for all observations. Approximate filter characteristics and camera QE were derived from manufacturer’s literature, with estimated peak QE = 60% for the front-illuminated CMOS detector. The z'2 long-pass filter was used instead of z\_s2 cutoff filter to maximize sensitivity. Right: filter equivalent center wavelengths, convolved with the ZWO ASI 1600MM camera QE.

For this exploratory phase of the project, no image calibration was done. Standard photometric practice (using dark, flat, and bias frames to calibrate both the speckle and long exposures) should improve photometric accuracy. This would probably improve the component flux proportions, color indexes, and spectral type correlations presented below.

### 3. KR 60AB Example

The eight steps of the speckle photometry method were first applied to the nearby red dwarf binary WDS 22280+5742 = KR60AB. WDS gives V magnitudes of 9.93 + 11.41 and spectral types M3.5V + M4.5V. Results from KR60AB observations are provided in each of the eight subsections below to illustrate the eight steps in the method.

#### 3.1 Normal Speckle Observations

A binary star is observed with normal speckle techniques, consisting of many short exposures for each filter, as well as observation of a single reference star. Bispectrum Analysis (BSA), also known as triple correlation, is performed on the images. The reference star images are used in deconvolution, removing optical aberrations that appear in both the binary and single star images. BSA processing of the sequence of many short exposures yields a reconstructed, diffraction-limited image of the binary star, from which astrometric measurements of separation and position angle are made. BSA images of KR60AB are shown in Figure 3.



Figure 3. Bispectrum Region of Interest images from the first set of observations of KR60AB, with East left, North up. The images are 128x128 pixels (22"x22") in size. Left to right: Sloan g' r' i' z' bands. Combining five sets of observations across all four filters yielded an average (and standard error of the mean) for separation  $\rho = 2.043'' \pm 0.020''$  and position angle  $\theta = 208.00 \pm 0.49$  degrees. This red dwarf pair is relatively faint in g' and even in r', but is still bright in z', even though camera QE has fallen off.

Image scale (arc-sec/pixel) and camera orientation on the sky were measured by plate solving several full-frame images of the area around the target on each night. Plate solving is incorporated into the SiTech control software and is the standard speckle calibration procedure at FIRO. Plate solving produces remarkably accurate and consistent calibration results, much better than the drift calibration method used in earlier speckle observations (Wasson, 2020).

All speckle analysis is done with the Speckle Tool Box (STB) software (Rowe, 2020). It is important to use the speckle analysis tools and parameters within STB in a consistent way, especially for photometry-related measurements, to keep from introducing small but unnecessary differences among the observations.

### 3.2 Flux Proportions

Approximate signal/noise ratio (S/N) for the five sets of Bispectrum analysis (BSA) images are shown in Figure 4 in the time sequence taken. Because of the low dark current and read noise of the CMOS camera, it is believed that the dominant noise sources of the speckle BSA images are variable extinction and shot noise.

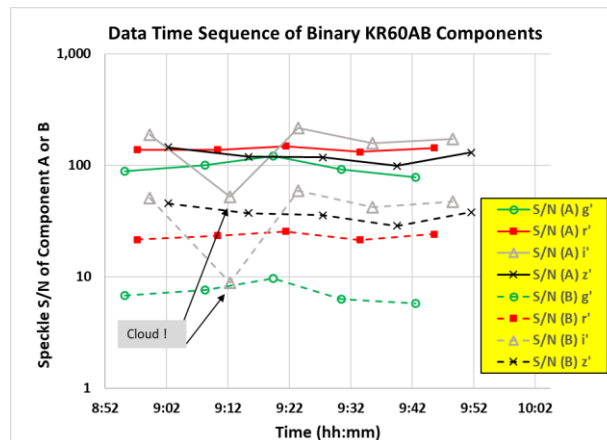


Figure 4. Time sequence of S/N for the binary components in BSA reconstructed images. The large dip in both A and B during the second set, occurring only in the i' filter, was probably caused by a small cloud or jet contrail.

In Figure 4, the four solid lines are the A (primary) star, and the four dashed lines are the B (secondary) star. Note the large dip in both A and B during the 2nd set, which occurred only in the i' filter. This was apparently caused by a small cloud or jet contrail briefly drifting by during some of the 1000 frames. The time sequence of the long exposures showed no such dips.

Since the BSA reconstructed image approaches zero wavefront error, it contains approximately correct flux which is used to extract the *flux proportion* of each component from the image. In addition to the usual

astrometric  $\rho$  and  $\theta$  measurements, flux proportion is the only photometric product of the resolved BSA images shown in Figure 3.

In the BSA images, both stars have the same point spread function (psf), but rise above the background by different levels, making them appear to have different sizes. The same photometric aperture must be used for flux measurement of each component, and the aperture is sized to fit closely around the fainter star to avoid including background noise. Even though the small aperture may appear too small for the brighter star, using the same aperture means that the same percentage of total psf flux (and consistent magnitudes) are measured for both stars. Flux Proportion (FP) is defined in equation (1), where either ADU or photo electron signals give the same results. The sum of the A + B proportions is always 100%.

$$FP_A = ADU_A / (ADU_A + ADU_B) \quad FP_B = ADU_B / (ADU_A + ADU_B) \quad (1)$$

Although the S/N data in Figure 4 seem quite ragged—even without considering the “cloud”—the BSA reconstructed images produced good repeatability and smooth trends in the FP for each component, as seen in Figure 5. The  $i'$ -band dips are plotted as “x” symbols there; this dimming apparently diverted a greater proportion of light away from the B star than from the A star in the BSA solution. In further analysis for each band the average FP of the five sets was used, but only 4 sets in  $i'$ , neglecting the “cloud” data.

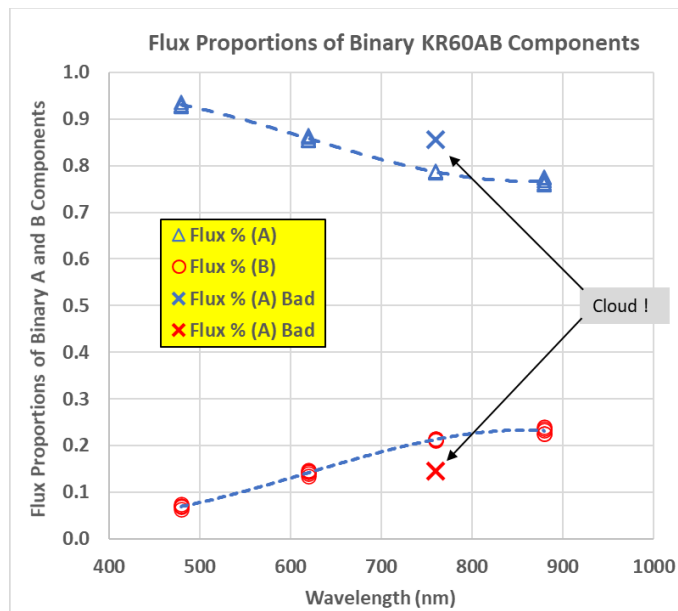


Figure 5. Flux proportions of the A and B components of KR60AB, produced by aperture photometry of the five sets of BSA images in the  $g' r' i' z'$  bands. Repeatability is good, except for the cloud-affected image, which was ignored in further analysis. Data for the  $g' r' i' z'$  filters are plotted at their respective center wavelengths given in Figure 2.

### 3.3 Long Exposures

Deep CCD exposures of the binary itself, taken in all-sky Surveys such as SDSS, Pan-STARRS, and APASS, provide standard Sloan photometric magnitudes of the unresolved binary star. During long exposures in the speckle photometry method, the atmosphere mixes the close binary components into an unresolved seeing disk, just as it does in the survey images. In this way, the long exposures provide a means of self-calibration, without the need to observe a separate comparison star.

After speckle exposures for one filter are completed (typically several hundred to a thousand), the binary is immediately observed with 10 long exposures. These are about 10 to 20 times longer than the speckle exposures, using the same filter and camera Region of Interest (RoI). The long exposures enable atmospheric

jitter to smear out the binary image to become a seeing-limited single star. Multiple images are taken and stacked to achieve high S/N, while avoiding tracking error drift.

The long exposures are interleaved immediately after each group of speckle frames to make the exposures as near in time as possible within each filter, thus minimizing the time for significant variations of the atmospheric noise to develop, especially variable extinction. The interleaved sequences are observed in this order:

g' speckle, g' long      r' speckle, r' long      i' speckle, i' long      z' speckle, z' long

This constitutes one “set” of observations: a sequence of speckle and long exposures in all filters. To assess repeatability statistics of the astrometric and photometric results, several sets of observations were made (three to six sets were typically acquired), composing a single nightly observation. Five KR60AB sets were observed on the first night.

This approach is a variation on the common practice of differential photometry of variable stars, but without the wider field needed to include comparison and check stars in CCD imaging. The long exposures of the target binary itself, using the same RoI, play the role of a “secondary standard” comparison star, providing a way to adjust the instrumental magnitude to the magnitude on a standard system.

It may be possible to eliminate the long calibration exposures by processing the speckle exposures in a different way, in addition to BSA: stacking all the short speckle exposures to create a single long exposure with an equivalent unresolved atmospheric seeing disk. This would save observation time but would require care in centroiding to account for telescope tracking drift. This technique could be explored in the future.

The long images are stacked to produce a single image with high S/N and a more symmetric psf. The flux is measured with a photometric aperture suitable for the seeing disk, much larger than for the two stars in the BSA image. Wide separation may lead to asymmetric star images, but a larger photometric aperture can still include all the light, albeit with added background noise. The atmosphere will usually blend the components well enough, up to  $\rho < 3''$ . The same aperture, large enough to include all the light in all four bands, is desirable for consistency of color index calibration. It is also needed to account for longer wavelengths having a larger psf, although atmospheric blurring is usually reduced (better seeing at long wavelengths). The relative brightness of A and B may also change the asymmetry among filters.

It is assumed that neither component of the binary is a variable star. However, small-amplitude variability is common and constitutes an added noise source. If one component were a variable star with large amplitude, i.e., well above the noise of photometric calibration, it might be possible to determine its approximate light curve over a series of observations.

### 3.4 Photometric Self-Calibration

In our preliminary evaluation of this speckle photometry method, standard photometric image calibration using flat, dark, and bias frames was not done. Therefore, some noise is present which could have been suppressed by careful calibration. However, a small RoI (256x256 pixels) was used, so the star was always near the camera field center even though not guided. Also, the CMOS camera has low dark current and low read noise. Recording 300 to 1000 speckle frames for each filter, typical of speckle practice, helps reduce noise. Therefore, shot noise, especially for faint secondary components, is likely the dominant noise source.

The long exposure images were not processed, except for stacking to create a single high S/N image for each filter. The same aperture, as noted above, was used in STB to measure long-exposure flux in all four filters for consistency of color index calibration. The net ADU flux within the aperture was converted to photoelectrons per second, to account for camera gain and different exposure times for different filters. The instrumental magnitude of the unresolved binary was calculated from the net flux measured in the stacked long exposure, using equation (2).

$$m_{(A+B)} = -2.5 * \text{Log}_{10}(\text{Net Flux}_{A+B}) \quad (2)$$

For each filter, the instrumental magnitude ( $m$ ) was then compared with the standard magnitude ( $M$ ) from survey catalogs. The AAVSO APASS photometric survey catalog, Data Release10 (AAVSO, 2020), was generally used because it had brighter magnitude limits, included magnitudes for all four Sloan filters more consistently, and was more easily accessed than other large photometric surveys. A Calibration Factor (magnitude difference) was calculated per equation (3):

$$Z_{A+B} = (M_{\text{Standard}} - m_{\text{Instrumental}})_{A+B} \quad (3)$$

This simple calibration factor includes instrumental transformation to the standard system, so it is valid for only one filter at a time. It also includes the variable atmospheric extinction terms which impact photometry: air mass, sky transparency and extinction effect on color. Since the sky may vary rapidly, frequent “recalibration” is assumed to be required; therefore, a new series of long exposures is observed for every series of speckle frames. The calibration factors for each filter, noted as  $Z$  in equation (3), are the final product of the long exposures, and are shown in Figure 6, where all five points lie closely together in the  $r'$  band (624 nm), which has the highest S/N.

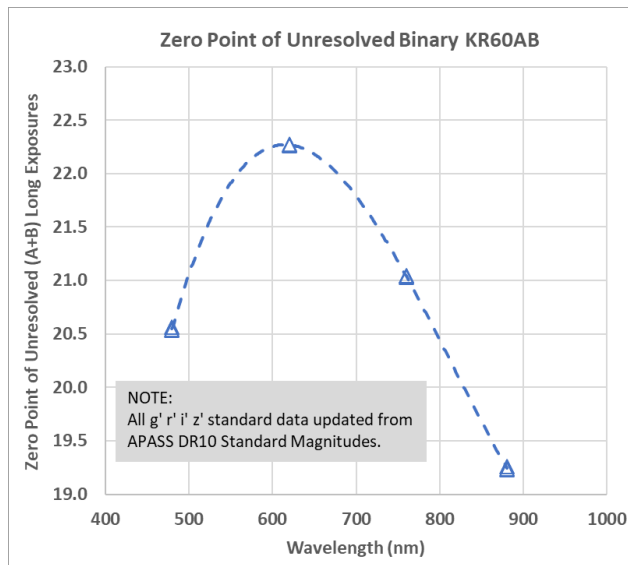


Figure 6. The calibration factors (“zero Points”) for KR60AB had good repeatability for the five sets of long unresolved exposures.  $Z$  is defined as the magnitude difference: APASS10 Standard magnitude - Instrumental magnitude, equation (3).

The long exposures are the only photometric calibration used in this method, i.e., they *define* the calibration factors which transform the unresolved star instrumental magnitude to the standard Sloan system. In some ways the calibration factors are analogous to the zero points of all-sky photometry; however, they are only a short-cut global approximation of the combined photometric correction terms, rather than a rigorous determination of extinction corrections and instrumental transformation from standard star measurements. In effect, the binary star itself is treated as a secondary standard star for self-calibration.

The calibration factors in Figure 6 are intended to account approximately for all photometric errors, both constant (e.g., filter/detector transformations) and transient (e.g., extinction). This approach is something like differential photometry, where the long exposures play the role of a comparison star to adjust an instrumental magnitude to a standard system magnitude. In the spirit of differential photometry, a better technique could take long exposures both before and after the speckle frames, then use the average to get the calibration factor, overlapping the time and conditions of the speckle frames.

A key assumption is that the calibration factor, which is measured from the unresolved *combined* light of both components, may be applied to the *individual* A and B stellar components. This assumption seems

reasonable for similar stellar types and colors, but it may cause systematic errors in the B star for high delta magnitude binaries, where the primary star dominates the long exposures but A and B have much different colors and S/N.

### 3.5 Component Standard Magnitudes

To estimate the instrumental flux of the binary A and B components, equation (4), the combined flux measured from the stacked long exposures is simply multiplied by the flux proportion (FP, equation 1) of each component measured from the reconstructed BSA image.

$$\text{Net Flux}_A = \text{Net Flux}_{A+B} * \text{FP}_A \quad \text{Net Flux}_B = \text{Net Flux}_{A+B} * \text{FP}_B \quad (4)$$

The instrumental magnitude of each component is then calculated from equation (5).

$$m_A = -2.5 * \text{Log}_{10}(\text{Net Flux}_A) \quad m_B = -2.5 * \text{LOG}_{10}(\text{Net Flux}_B) \quad (5)$$

Finally, the standard magnitudes of the components are estimated simply by adding the calibration factor back to their instrumental magnitudes, equation (6). This key assumption of the method bears restating: although the calibration factor is *derived from the unresolved star*, it is *applied to each component* of the binary separately, to estimate its standard magnitude.

$$M_{A \text{ Standard}} = m_{A \text{ Instrumental}} + Z_{A+B} \quad \text{and} \quad M_{B \text{ Standard}} = m_{B \text{ Instrumental}} + Z_{A+B} \quad (6)$$

The resulting estimated standard magnitudes for the components of KR60AB are shown in Figure 7. The magnitudes of the A star are reasonably consistent with the APASS10 survey, but the B component is significantly fainter. The WDS magnitudes (presumed to be Johnson V) are 9.93/11.41, or  $\Delta\text{mag} \sim 1.5$ . At the V filter center WL ( $\sim 540\text{nm}$ ) the speckle photometry estimated  $\Delta\text{mag}$  is  $\sim 2.4$ , almost a full magnitude fainter.

After the observations were made, it was found that the B component is the known flare star DO Cep, with a visual range  $>1$  magnitude (combined light of both components); if the variability is mainly from the B component, its range may be  $>2$  magnitudes. APASS10 data has uncertainties less than 0.06 magnitude in the 2 to 4 observations in each filter for this star. It seems unlikely that it was observed by APASS only during several similarly brightened episodes; however, the long-term AAVSO light curve does show sustained periods of roughly constant brightness.

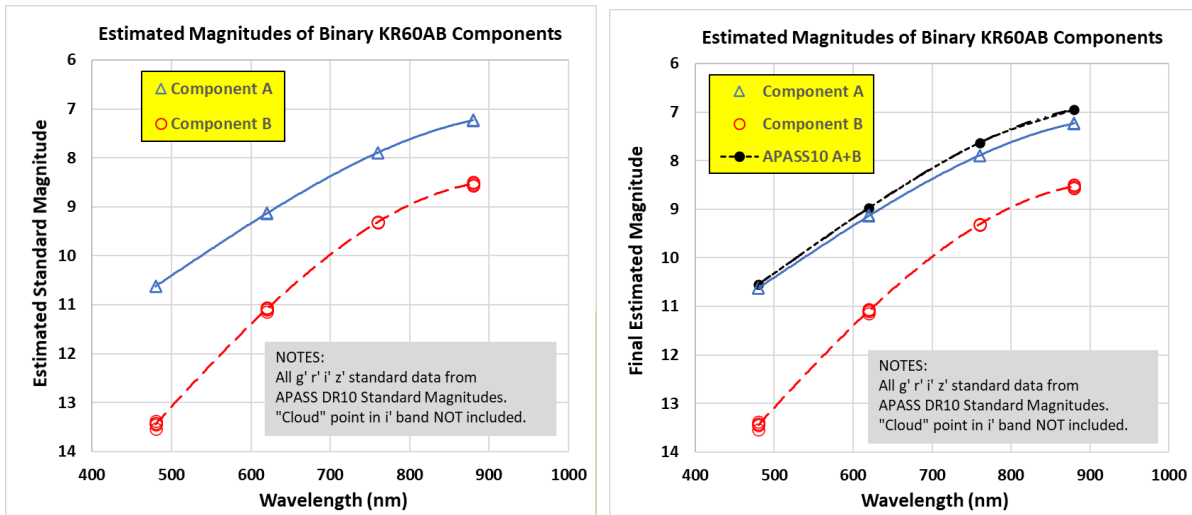


Figure 7. Left: speckle photometry estimated standard  $g' r' i' z'$  magnitudes of the A and B components, based on the flux proportions of Figure 5 and the calibration factors of Figure 6. Right: added standard magnitudes of APASS10 (combined light), which are slightly brighter than the A component, as expected.

### 3.6 Component Color Indexes

Color index is the difference in standard magnitude between any two filters. Measuring color indexes of the A and B components of a binary star on the standard Sloan photometric system is a major goal of this speckle photometry method. Therefore, the filters must be grouped together in a set of all four filters observed with their long calibration exposures close together in time, as described in Sections 3.3 and 3.4. Three to six sets of filters were observed, each set considered as a sample independent from the other sets, to assess photometric uncertainty and identify outliers. Color indexes are calculated from the filters within each set, and overall nightly color indexes are taken from the average magnitudes of all sets.

Six color indexes are formed from the four  $g'$   $r'$   $i'$   $z'$  filters:  $(g'-r')$ ,  $(g'-i')$ ,  $(g'-z')$ ,  $(r'-i')$ ,  $(r'-z')$ , and  $(i'-z')$ . Although all six are equally valid, an error in any one standard magnitude will propagate into three of the color indexes.

Most photometric correction terms will tend to cancel in this method, as they do in differential photometry, where the variable and comp stars are observed under nearly the same conditions. However, the 2<sup>nd</sup>-order (color) extinction term is not trivial for stars of different colors, particularly for a binary consisting of an early primary and a late secondary star. The 2<sup>nd</sup>-order correction is not well accounted for in this method because it includes the color index times airmass; color index is large for red stars, and airmass is never less than 1. This is analogous to using a comparison star of much different color in differential photometry. Therefore, this term may add a systematic error to the color indexes of a blue-red binary, particularly to the redder star.

Color Indexes are compared in Figure 8, plotted in order of a “normalized wavelength” parameter which is simply the difference in center wavelength (WL) between any two filters, divided by their average WL. The normalized WL places the color indexes roughly in order of increasing sensitivity, corresponding generally to the separation of the filters.

For late red stars, such as both components of KR60AB, the color indexes are large and have a roughly linear character seen in Figure 8, but the primary star follows the APASS10 trend much more closely than the secondary star. The more pronounced secondary star “bump” at the  $r'-z'$  index is not understood; it may simply be noise, or an artifact of photometric transformation among broadband filters, or it could have astrophysical meaning, perhaps related to the molecular absorption bands that appear in cool, red stars.

The standard deviations for the speckle photometry color index data plotted in Figure 8 are reasonably small:  $A < 0.02$ ,  $B < 0.06$ , which are within the size of the plotted symbols. This is probably due to the frequent self-calibration with unresolved observations adjusted to APASS10 data which had internal standard deviation errors  $< 0.06$  magnitude. The standard deviations from APASS10 and the speckle photometry observations are added together as a conservative estimate of the internal error:  $A \sim 0.08$ ,  $B \sim 0.12$  magnitude. This is comparable with uncertainties estimated by Horch et al. (2001 & 2004) for small telescopes.

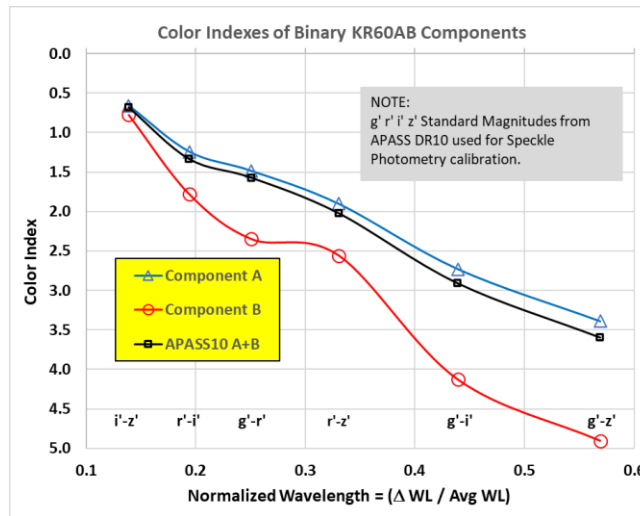


Figure 8. Example of color indexes from the APASS10 photometric survey and the speckle photometry method. The normalized wavelength parameter accounts for both WL difference and the WL region in which the difference occurs. The primary star closely follows the APASS10 trend, while the secondary has a significantly different character.

### 3.7 Reference Star

Somewhere among the repeated sets, a single reference star is observed in each filter. The reference star is used in standard speckle deconvolution processing to normalize the effects of optical aberrations on spatial information in the speckle frames, sharpening the bispectrum image results. No long exposures are required for the reference star since it is not involved in extracting photometric information. The only requirement for a reference star is that it should be single and brighter than the target binary star in all filters.

The reference star was only observed once for BSA deconvolution; it is best observed in the middle of the several photometric sets. For example, a complete nightly observation for one binary star, taking about 1 hour, might be:

Set1 (g r i z) Set2 (g r i z) Set3 (g r i z) Reference (g r i z) Set4 (g r i z) Set5 (g r i z)

### 3.8 Component Spectral Types

The foundation of spectrophotometry was laid by correlating Johnson U B V photometry color indexes with the spectra of Morgan-Keenan spectroscopic standard stars (Johnson & Morgan, 1953). As detectors became more red-sensitive, the correlation was extended to the Johnson-Kron-Cousins U B V Rc Ic bands. These J-C color index relationships to spectral type were refined to a continuous set by Pecaut & Mamajek (2013), then further refined, expanded, and made accessible on the web site of Mamajek (2019), which was the source for this work.

A photometric transformation was required from Johnson-Cousins B V Rc Ic magnitudes to the Sloan g' r' i' z' system; the transformation set of Rodgers, et al. (2006) was used, Table 2.

Table 2. The equations transforming Johnson-Cousins B V Rc Ic photometry bands to Sloan g' r' i' z' bands.

Rogers et al (2005) Transformations from J-C to Sloan for Main Sequence Stars, Unreddened
$g' = V - 0.042*(B-V)^2 + 0.602*(B-V) - 0.087$
$g'-r' = 0.278*(B-V) + 1.321*(V-Rc) - 0.219$
$r'-i' = 1.000*(Rc-Ic) - 0.212$
$r'-z' = 1.567*(Rc-Ic) - 0.365$

The spectrophotometric tables of Mamajek, transformed from Johnson-Cousins B V Rc Ic bands to Sloan color indexes, are plotted in Figure 9. Each of the six color indexes has a unique and equally valid relationship with spectral type. The data are continuous and monotonically increase with spectral type (and with the corresponding numerical parameter at bottom, used for ease of calculation).

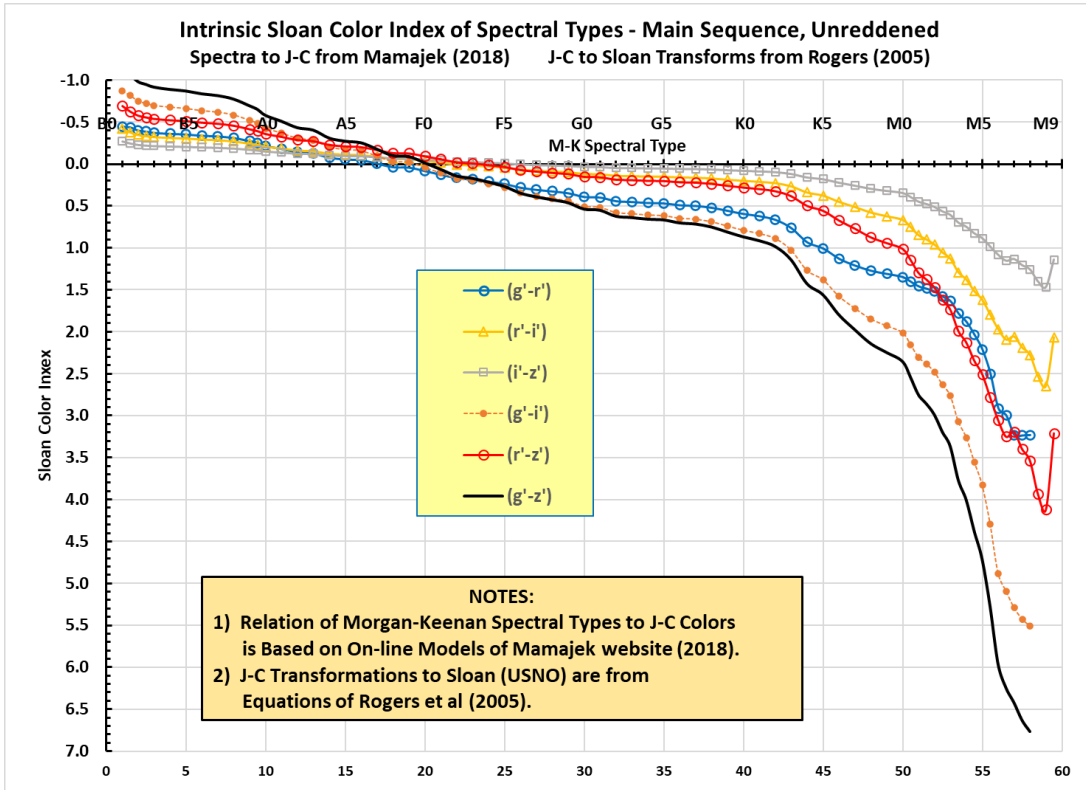


Figure 9. The relationship of Sloan filter color Indices to spectral type for main sequence dwarf stars. Spectral type is indicated at top. Each integer of the linear numerical parameter at bottom corresponds to an integer of spectral type (e.g., 30=G0, 31=G1, 32=G2, ...). This parameter is used to interpolate spectral type from measured color index.

The Mamajek tables are limited to normal dwarf stars on the main sequence that are near enough to the Sun that they are not significantly reddened by interstellar dust. The spectral types are uniformly divided into a sequence of sub-types from B0 through M9. By interpolation of the measured color index versus the numerical spectral parameter, each measured Sloan color index provides an estimate of spectral type.

Figure 9 shows that each color index has a different sensitivity to spectral type. A smaller variation with spectral type would have a greater uncertainty for the same  $\Delta$  magnitude measurement accuracy. Therefore, the approximately linear slope (spectral sensitivity) in the range from A0 to K0 is used as a weighting factor for its color index, when calculating the weighted average spectral type of each binary component star. These sensitivity slopes are given in Table 3. There are many possible alternative weighting methods, but others were not explored.

Table 3. The sensitivity of color index to spectral type, derived from Figure 9. Slopes are defined as the difference in Color Index between types A0 and K0, divided by the difference in the numerical spectral parameter (40-10=30). The i'-z' Color Index, orange, is smallest, least sensitive to spectral type, and most subject to photometric errors.

Color Index Weighting Factors (A0-K0 Slope)			
Index	A0	K0	Slope
g'-r'	-0.218	0.593	0.0270
r'-i'	-0.209	0.198	0.0136
i'-z'	-0.151	0.079	0.0077
g'-i'	-0.427	0.791	0.0406
r'-z'	-0.360	0.277	0.0213
g'-z'	-0.578	0.871	0.0483
Average Slope:			0.0264

The way that spectral type is calculated from color indexes is shown by the example spreadsheet in Table 4. The numerical parameter at the bottom of Figure 9 is linearly interpolated at the measured color index from the Mamajek data. The parameters are weighted by their respective spectral sensitivities (i.e., the slopes in Table 3) to provide the weighted average parameter. The “Std Error” is the standard deviation of the parameters divided by the square root of the number of samples, which is chosen as 4, the number of filters originally observed. However, for small samples of an unknown (perhaps non-normal) population, this uncertainty may be underestimated; standard deviation (i.e., twice the Std Error shown) would be a still more conservative uncertainty estimate. Estimated Spectral Type for A and B is the final product of the spreadsheet.

Table 4. The KR60AB Spectral Type calculation from Color Indexes by interpolation of the linear spectral parameter at the bottom of Figure 9. Average is the weighted average. Range is average +/- standard error. Spectral types in the bottom two rows were manually looked up from the Mamajek tables.

Estimated Spectral Types - from Speckle Photometry						APASS 10		
KR60A: WDS Spect = M3.5V			KR60B: WDS Spect = M4.5V			KR60AB: Combined		
Estimated Spectral Type			Estimated Spectral Type			Estimated Spectral Type		
Color Index	Measured Index	Interpolated Parameter	Color Index	Measured Index	Interpolated Parameter	Color Index	Measured Index	Interpolated Parameter
g'-r'	1.486	51.5	g'-r'	2.349	55.2	g'-r'	1.574	52.5
r'-i'	1.243	53.4	r'-i'	1.780	55.5	r'-i'	1.337	53.8
i'-z'	0.660	53.3	i'-z'	0.777	54.2	i'-z'	0.686	53.4
g'-i'	2.729	52.9	g'-i'	4.128	55.3	g'-i'	2.911	53.2
r'-z'	1.903	53.3	r'-z'	2.556	55.1	r'-z'	2.023	53.6
g'-z'	3.389	53.0	g'-z'	4.905	55.2	g'-z'	3.597	53.3
Average:		52.8	Average:		55.2	Average:		53.2
Std Error:		0.4	Std Error:		0.2	Std Error:		0.2
Range:	52.5	53.2	Range:	55.0	55.4	Range:	53.0	53.5
<b>Estimated Type: M2.8V</b>			<b>Estimated Type: M5.2V</b>			<b>Estimated Type: M3.2V</b>		
<b>Type Range: M2.5 - M3.2</b>			<b>Type Range: M5.0 - M5.4</b>			<b>Type Range: M3.0 - M3.5</b>		

Table 4 also includes the color indexes and corresponding spectral types for the combined light measured by APASS10. The color indexes are between the two components, closer to the primary star, as they should be. Likewise, overall spectral type and range are close to the primary but shifted slightly toward the B star. These results are a direct result of using APASS10 data to standardize the observed magnitudes.

Table 5 summarizes the Spectral types of the KR60AB component stars, estimated from the speckle photometry method, compared with those of the WDS Catalog. The spectral types are in good agreement.

Table 5. Spectral types of the A and B components of KR60AB estimated by the Speckle Photometry method on the first night of observation, compared with the spectral types given in the WDS Catalog.

	Component A	Component B
Speckle Photometry	M2.8V	M5.2V
WDS	M3.5V	M4.5V

To further illustrate the correlation of color index with spectral type, Figure 10 shows the same color index curves as Figure 9, but with KR60AB measured data added in the inset table. Also added are color-coded arrows which extend from the spectral-type axis to each corresponding color index curve. For clarity, the arrows are only shown for the primary A component of KR60AB. The 6 arrows nearly overlay one another, showing how the large variations of color index correspond to nearly the same spectral type. The  $g'-r'$  index (blue arrow) is an outlier, but its influence is moderated by the averaging process.

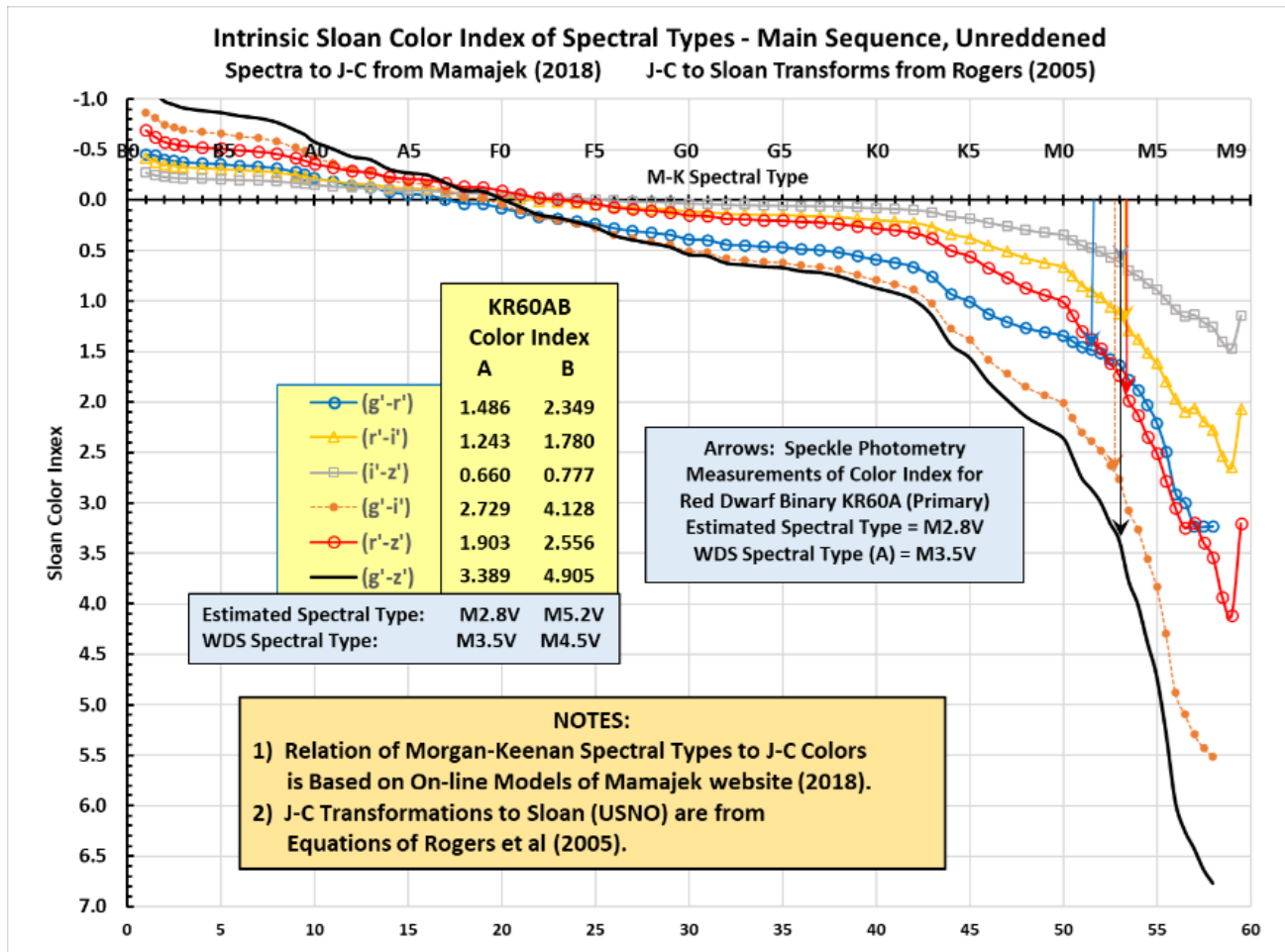


Figure 10. The relationship of Sloan color indexes to spectral type, the same as Figure 9 above. The example of KR60AB measured speckle photometry color indexes and resulting estimated spectral type is shown in the inset table. Color-coded arrows, some of which nearly overlay one another, indicate the six estimates of the individual color indexes for the A component; all except  $g'-r'$  are in excellent agreement.

## 4. Summary of Key Assumptions

The method's six key assumptions are:

- Speckle bispectrum analysis produces the correct flux proportions for binary star components.
- The simple global calibration factor, derived from photometry of the unresolved binary in long exposures, fully transforms instrumental magnitudes to standard Sloan magnitudes.
- The calibration factor, derived from combined light of both components, is also valid for the A and B binary components individually, but may introduce systematic errors for early-late binary components.
- Accurate photometry of large surveys provides secondary standard stars with small errors.
- Variability of one or both components would impact the standard magnitude and color index correlations. However, large variability of one component may be detectable over a series of observations.
- The correlations of spectral type with Johnson-Cousins color indexes in the Mamajek tables are still valid when transformed to the Sloan photometric system.

## 5. KR60AB Night-to-Night Repeatability

In this section, speckle photometry repeatability results are presented for KR60AB, which was observed on three nights during 2020: Oct 20, Oct 31, and Dec 4. On each night, all four filters were used, and 5, 3, 3 sets of speckle plus long exposures were observed, respectively.

Figure 11 presents the variations of flux proportions for the three nights, measured from speckle BSA images. The FP trends are consistent, but there are shifts of several percent in the A and B proportions. Since there is good repeatability of the sets within each night, these shifts may be caused by night-to-night atmospheric variations in temperature, extinction, etc. However, the differences could also represent intrinsic variability of the B component, flare star DO Cep.

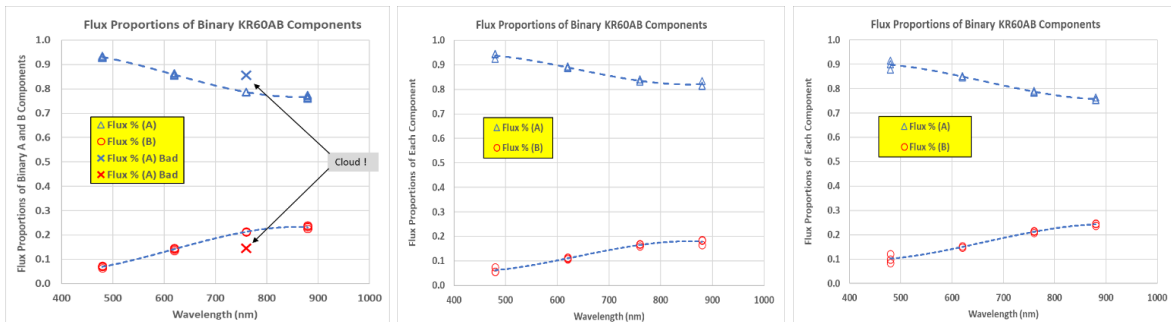


Figure 11. The flux proportions measured for the A and B components of KR60AB from speckle BSA reconstructed diffraction limited images. The observations were in 2020 on 20 Oct (left), 31 Oct (middle) and 4 Dec (right).

The calibration factors derived from the long unresolved exposures of KR60AB for the three observing nights are presented in Figure 12. These calibration data show large variations from night-to-night, up to several magnitudes in  $g'$ , primarily because of variable atmospheric transparency and airmass. Such highly variable first and second order extinction is the primary reason for obtaining the calibration data, which enables adjustment of the speckle BSA flux proportions to the standard Sloan photometric system.

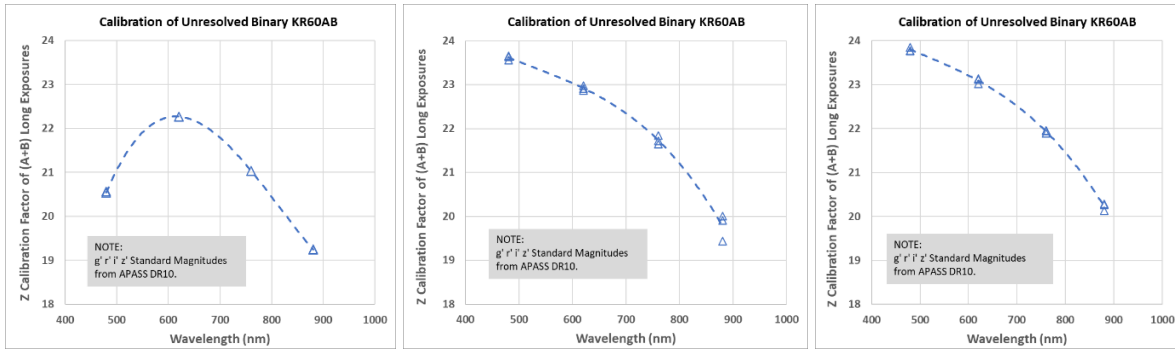


Figure 12. Calibration Factors measured for the unresolved long exposures of KR60AB on 20 Oct 2020 (left), 31 Oct 2020 (middle) and 4 Dec 2020 (right).  $Z = M_{APASS10} - m_{Long Exposure}$ .

The standard Sloan magnitudes of the KR60AB components measured by the speckle photometry method are presented in Figure 13 for the three observed nights. The primary star is reasonably constant, while the secondary star shows more variation. This may be caused by intrinsic variability, seen as a shift and/or rotation of the trends. However, it could also be caused by variable 2<sup>nd</sup>-order (color) extinction. Lower S/N for the B star also contributes, indicated by more scatter within a night, especially for the g' and z' filters, where the star is faint or the QE is low, respectively.

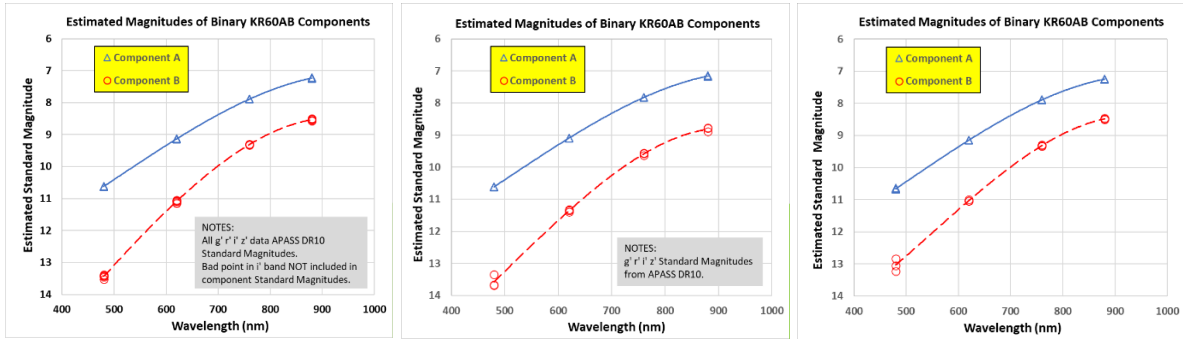


Figure 13. Standard Sloan magnitudes for KR60AB on 20 Oct 2020 (left), 31 Oct 2020 (middle) and 4 Dec 2020 (right).

Details of night-to-night variation of standard magnitudes are shown in Table 6. Overall, the primary star magnitude uncertainty is  $<0.05$ ; variation of the secondary star, which may include slight intrinsic variability, is  $<0.3$  magnitude. The consistency of Figure 13, contrasted with the large variations in Figure 12, demonstrates the effectiveness of the “differential photometry” approach, but the best results are still obtained under a clear, steady photometric sky.

Table 6. Summary of measured standard magnitudes for the KR60AB components. The left-most column indicates the filter and its standard deviation within the night. For each date, the two columns are for components A (left) and B (right), respectively. The right-most two columns are standard deviations of the night-to-night observations.

KR60AB - Summary of Night-to-Night Standard Magnitudes								
	20 Oct 2020		31 Oct 2020		4 Dec 2020		A Std Dev	B Std Dev
g'	10.620	13.437	10.612	13.570	10.659	13.034	0.025	0.279
$\sigma_{g'}$	0.004	0.058	0.013	0.188	0.023	0.196		
r'	9.134	11.088	9.095	11.361	9.145	11.026	0.026	0.178
$\sigma_{r'}$	0.006	0.037	0.004	0.036	0.004	0.021		
i'	7.891	9.309	7.827	9.587	7.890	9.313	0.037	0.159
$\sigma_{i'}$	0.003	0.009	0.007	0.034	0.005	0.020		
z'	7.231	8.532	7.159	8.817	7.247	8.483	0.047	0.180
$\sigma_{z'}$	0.010	0.032	0.014	0.066	0.007	0.023		

Color indexes of the KR60AB components measured by the speckle photometry method are presented in Table 7 for the three nights. The uncertainties of the primary star within each night are generally several times smaller than for the secondary star, again likely due to the lower S/N of the fainter star. Night-to-night uncertainties are similar to those of the standard magnitudes from which they were derived, Table 6 above. The resulting estimated spectral types are remarkably consistent.

Table 7. Summary of measured color indexes and estimated spectral types for the KR60AB components. The left-most column indicates the color index and its standard deviation within the night. For each date, the two columns are for components A (left) and B (right), respectively. The right-most columns are standard deviations of the night-to-night color index observations. The bottom rows are the weighted average spectral parameter and the corresponding estimated spectral type.

KR60AB - Summary of Night-to-Night Color Indexes and Spectral Types								
	20 Oct 2020		31 Oct 2020		4 Dec 2020		A Std Dev	B Std Dev
i'-z'	0.660	0.777	0.668	0.770	0.644	0.830	0.013	0.033
$\sigma$	0.009	0.029	0.019	0.090	0.012	0.039		
r'-i'	1.243	1.780	1.268	1.774	1.254	1.714	0.013	0.037
$\sigma$	0.007	0.040	0.003	0.009	0.009	0.041		
r'-z'	1.903	2.556	1.936	2.544	1.898	2.544	0.021	0.007
$\sigma$	0.013	0.055	0.018	0.096	0.007	0.023		
g'-r'	1.486	2.349	1.517	2.209	1.514	2.008	0.017	0.171
$\sigma$	0.006	0.057	0.013	0.187	0.023	0.196		
g'-i'	2.729	4.128	2.785	3.983	2.768	3.721	0.029	0.206
$\sigma$	0.003	0.059	0.012	0.178	0.024	0.202		
g'-z'	3.389	4.905	3.453	4.753	3.412	4.551	0.033	0.177
$\sigma$	0.008	0.044	0.013	0.161	0.016	0.175		
Sp Param	52.8	55.2	53.0	55.1	52.9	54.8		
Spec Type	M2.8V	M5.2V	M3.0V	M5.1V	M2.9V	M4.8V		

## 6. Speckle Photometry Results for Other Binaries

Three additional binary stars were observed which had spectral types for both components in WDS. Their characteristics were given in Table 1 above. Together with the red dwarf results for KR60AB above, the components of these systems sample a broad range of spectral types: A F G K M. STF554 was observed on two nights of different photometric quality, as explained below. Several additional binaries were observed, but only on poor photometric nights, producing unusable results. The major products of the speckle photometry method are presented as they were for KR60AB, except that the same plots are shown together for all three binaries.

### 6.1 Flux Proportions

The flux proportions for the three additional binaries are shown in Figure 14. STF554, a very bright star (80 Tauri) was observed on two nights of different photometric quality, the second night at far right. The Fairborn Institute's Robotic Observatory, in its 2020 home in California prior to its move to Arizona, was located at moderate elevation about 20 miles from the Pacific Ocean. Cool moist breezes from the ocean, the marine layer, frequently dominate the California coast weather. Clear evenings are often spoiled by rising humidity and transient clouds that gradually increase to solid overcast.

In Figure 14 the three patterns of FP are caused by the different delta magnitudes between the AB components for the three binaries. There is a wide range of scatter in the flux proportions, mainly caused by variable extinction. The g', i' and z' bands seem most affected. When the binary is dimmed by high extinction, the secondary star data suffers most because its S/N declines dramatically. Since the sum of flux proportions for the two components is defined as 1.0, the primary star reflects the scatter in the secondary.

HLD60 has large scatter, especially in  $i'$  and  $z'$ . The case of STF554 on the right illustrates the impact of variable extinction. The third plot (January 15) was a typical night that started clear, but gradually deteriorated with increasing humidity. While the scatter is moderate, there is an odd, recurved trend with WL. The night of February 6 had the opposite weather pattern: high pressure, dry air, and no marine influence - a photometric night. The scatter is less, the secondary star is brighter, and the odd recurved trend with WL is absent.

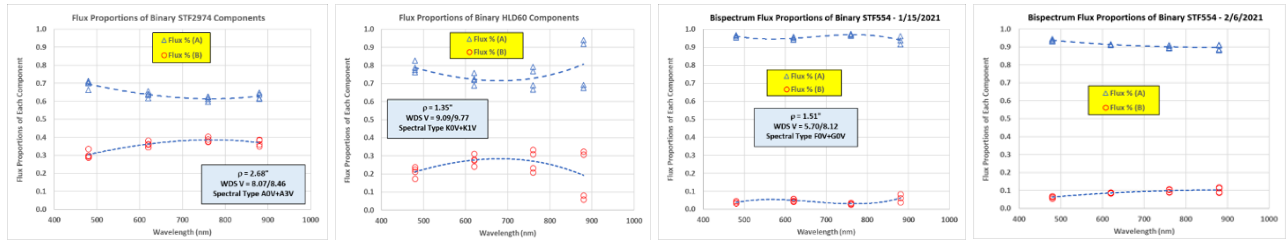


Figure 14. Left to right, the flux proportions measured for the A and B components of STF2974 (5 sets), HLD60 (4 sets), and STF554 observed on two dates (5 sets on 1/15/2021, 4 sets on 2/6/2021).

## 6.2 Calibration Factors

Calibration factors are shown in Figure 15. High scatter betrays the HLD60 and STF554 (1/15/21) results as suffering variable extinction. Good repeatability of the STF2974 and later STF554 (2/6/21) calibrations indicate steady extinction.

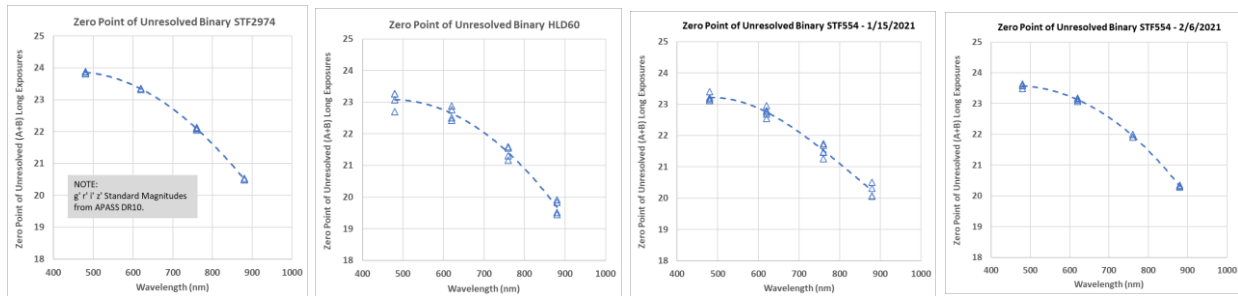


Figure 15. Left to right: the calibration factors measured for the A and B components of STF2974 (5 sets), HLD60 (4 sets), and STF554 observed on two dates (5 sets on 1/15/2021, 4 sets on 2/6/2021).

## 6.3 Standard Magnitudes

Figure 16 shows that the trends of the measured flux and calibration parameters are reflected in similar magnitude results. APASS10 standard magnitudes of the unresolved binary were generally used as the “truth model” for long exposure calibration. However, no APASS10 data were available for the binaries HLD60 and STF554 because they are too bright. GaiaDR2 resolved these binaries and provided G Bp Rp photometry data for both components. Therefore, the combined magnitudes of the A and B components from the ATLAS Catalog were used for calibration. The ATLAS All-Sky Stellar Reference Catalog (Tonry et al. 2018) and (Carrasco 2015) is a major product of Gaia DR2, containing photometric data transformed to other major photometric systems including the PanSTARRS version of the Sloan  $g'$   $r'$   $i'$   $z'$  bands.

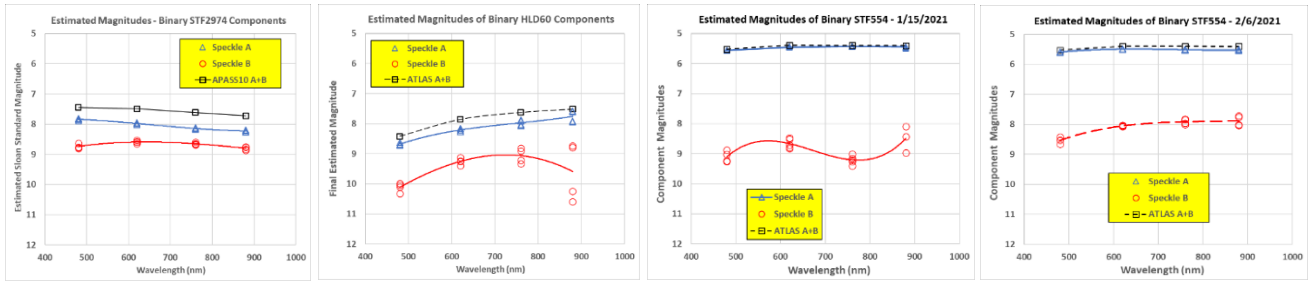


Figure 16. Left to right: standard magnitudes measured for the A and B components of STF2974 (5 sets), HLD60 (4 sets), and STF554 observed on two dates (5 sets on 1/15/2021, 4 sets on 2/6/2021).

### 6.4 Color Indexes

Color Indexes for components of the three binaries are shown in Figure 17. Color index results for the STF554 secondary star on 1/15/21 are erratic because of variable extinction. Much better quality is seen for the good sky conditions of 2/6/21.

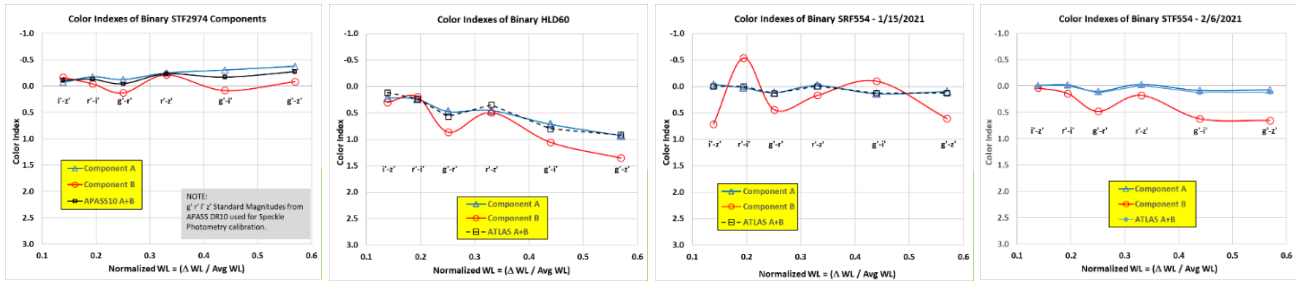


Figure 17. The Color Indexes measured for the A and B components of STF2974 (5 sets), HLD60 (4 sets), and STF55 observed on two dates (5 sets on 1/15/2021, 4 sets on 2/6/2021).

### 6.5 Estimated Spectral Types

Speckle photometry estimates of Spectral Type are compared with the WDS types in Table 8. The spectral types are remarkably consistent with those of WDS, especially considering the large scattering in some cases, discussed above. For HLD60 particularly, the B star z' ADU data for 2 of the 4 sets were grossly dimmed by high extinction (see extremely low points in Figure 14). These two points were excluded from the three affected color indexes (i'-z', r'-z', g'-z') and are noted in red in Table 8. For STF554, the erratic color index r'-i' = -0.542 (Figure 17) was beyond the range of the Mamajek tables, so provided no interpolated parameter; it is highlighted in orange in Table 8 and was not included in the Average and Std Error calculations.

Table 8. The Estimated Spectral Types measured for the A and B components of STF2974 (left, 5 sets); HLD60 (Middle, 4 sets); and STF554 (right) observed on two dates (5 sets on 1/15/2021, 4 sets on 2/6/2021).

Estimated Spectral Types - from Speckle Photometry						Estimated Spectral Types - from Speckle Photometry					
STF2974A: WDS Spect = A0V			STF2974B: WDS Spect = A3V			HLD 60A: WDS Spect = K0V			HLD 60B: WDS Spect = K1V		
Estimated Spectral Type			Estimated Spectral Type			Estimated Spectral Type			Estimated Spectral Type		
Color	Measured	Interpolated	Color	Measured	Interpolated	Color	Measured	Interpolated	Color	Measured	Interpolated
Index	Index	Index	Index	Index	Index	Index	Index	Index	Index	Index	Index
g <sup>1</sup> -r <sup>1</sup>	-0.126	13.0	g <sup>1</sup> -r <sup>1</sup>	0.127	21.1	g <sup>1</sup> -r <sup>1</sup>	0.472	35.2	g <sup>1</sup> -r <sup>1</sup>	0.861	43.6
r <sup>1</sup> -i <sup>1</sup>	-0.176	11.4	r <sup>1</sup> -i <sup>1</sup>	-0.045	19.7	r <sup>1</sup> -i <sup>1</sup>	0.239	42.3	r <sup>1</sup> -i <sup>1</sup>	0.191	39.5
i <sup>1</sup> -z <sup>1</sup>	-0.070	17.9	i <sup>1</sup> -z <sup>1</sup>	-0.168	9.2	i <sup>1</sup> -z <sup>1</sup>	0.214	45.8	i <sup>1</sup> -z <sup>1</sup>	0.299	48.2
g <sup>1</sup> -i <sup>1</sup>	-0.303	12.1	g <sup>1</sup> -i <sup>1</sup>	0.082	20.6	g <sup>1</sup> -i <sup>1</sup>	0.711	38.4	g <sup>1</sup> -i <sup>1</sup>	1.052	43.1
r <sup>1</sup> -z <sup>1</sup>	-0.246	13.6	r <sup>1</sup> -z <sup>1</sup>	-0.213	15.0	r <sup>1</sup> -z <sup>1</sup>	0.452	43.6	r <sup>1</sup> -z <sup>1</sup>	0.490	43.9
g <sup>1</sup> -z <sup>1</sup>	-0.373	13.3	g <sup>1</sup> -z <sup>1</sup>	-0.086	19.0	g <sup>1</sup> -z <sup>1</sup>	0.925	41.1	g <sup>1</sup> -z <sup>1</sup>	1.351	43.7
Average:		13.1	Average:		18.8	Average:		40.1	Average:		43.4
Std Error:		1.1	Std Error:		2.3	Std Error:		1.9	Std Error:		1.4
Range:	11.9	14.2	Range:	16.5	21.1	Range:	38.2	42.0	Range:	42.0	44.8
Estimated Type:	A3.1V		Estimated Type:	A8.8V		Estimated Type:	K0.1V		Estimated Type:	K3.4V	
Type Range:	A1.9 - A4.2		Type Range:	A6.5 - F1.1		Type Range:	G8.2 - K2.0		Type Range:	K2.0 - K4.8	

Estimated Spectral Types - STF554 1/15/2021						Estimated Spectral Types - STF554 2/6/2021					
STF554A: WDS Spect = F0V			STF554B: WDS Spect = G0V			STF554A: WDS Spect = F0V			STF554B: WDS Spect = G0V		
Estimated Spectral Type			Estimated Spectral Type			Estimated Spectral Type			Estimated Spectral Type		
Color	Measured	Interpolated	Color	Measured	Interpolated	Color	Measured	Interpolated	Color	Measured	Interpolated
Index	Index	Index	Index	Index	Index	Index	Index	Index	Index	Index	Index
g <sup>1</sup> -r <sup>1</sup>	0.116	20.8	g <sup>1</sup> -r <sup>1</sup>	0.437	31.9	g <sup>1</sup> -r <sup>1</sup>	0.102	20.5	g <sup>1</sup> -r <sup>1</sup>	0.481	35.6
r <sup>1</sup> -i <sup>1</sup>	0.018	23.2	r <sup>1</sup> -i <sup>1</sup>	-0.542	#N/A	r <sup>1</sup> -i <sup>1</sup>	-0.019	20.9	r <sup>1</sup> -i <sup>1</sup>	0.139	32.3
i <sup>1</sup> -z <sup>1</sup>	-0.041	21.1	i <sup>1</sup> -z <sup>1</sup>	0.709	53.6	i <sup>1</sup> -z <sup>1</sup>	-0.011	24.8	i <sup>1</sup> -z <sup>1</sup>	0.034	30.3
g <sup>1</sup> -i <sup>1</sup>	0.133	21.4	g <sup>1</sup> -i <sup>1</sup>	-0.105	16.8	g <sup>1</sup> -i <sup>1</sup>	0.082	20.6	g <sup>1</sup> -i <sup>1</sup>	0.620	35.1
r <sup>1</sup> -z <sup>1</sup>	-0.023	22.0	r <sup>1</sup> -z <sup>1</sup>	0.167	31.4	r <sup>1</sup> -z <sup>1</sup>	-0.030	21.8	r <sup>1</sup> -z <sup>1</sup>	0.173	31.6
g <sup>1</sup> -z <sup>1</sup>	0.093	21.3	g <sup>1</sup> -z <sup>1</sup>	0.604	31.7	g <sup>1</sup> -z <sup>1</sup>	0.072	21.1	g <sup>1</sup> -z <sup>1</sup>	0.654	33.7
Average:		21.5	Average:		31.5	Average:		21.1	Average:		33.8
Std Error:		0.4	Std Error:		6.6	Std Error:		0.8	Std Error:		1.0
Range:	21.1	21.9	Range:	24.9	38.1	Range:	20.3	21.9	Range:	32.8	34.8
Estimated Type:	F1.5V		Estimated Type:	G1.5V		Estimated Type:	F1.1V		Estimated Type:	G3.8V	
Type Range:	F1.1 - F1.9		Type Range:	F4.9 - G8.1		Type Range:	F0.3 - F1.9		Type Range:	G2.8 - G4.8	

## 7. Astrometry Results

The astrometry results for the speckle photometry observations are summarized in Table 9. STB measurement tools use a set of circular apertures to measure the centroid positions of both stars and to sum the ADU flux within the apertures. For astrometry, different size apertures may be used with little effect on centroids. However, for photometry, the same size apertures are required for both stars, to measure the same *proportion* of light from each star, since they both have the same point spread function. The background level is measured in a separate aperture, rather than in an annulus, and is subtracted from the flux of each star.

For analysis, the astrometry and photometry results from each filter and all the repeated sets of filters—constituting a complete night’s observation—were copied to a series of Excel spreadsheets along with significant observational and measurement settings. The spreadsheets each dealt with one of the major products of the investigation: speckle astrometry, speckle and long exposure photometry, and estimated component spectral types. The spreadsheets provided a convenient format for consistent analysis, calculation of statistics, and plotting.

Table 9. Summary of astrometric measurements. The columns are date, WDS coordinates and discovery designation, Sloan filter, average position angle and standard deviation, average separation and standard deviation, speckle exposure time, number of speckle frames recorded in each set, and number of repeated sets of observations. For  $\theta$  and  $\rho$ , the statistics are for the number of sets (observations) in each filter. At bottom in yellow are the overall average and standard deviation, combining all filters and all sets of observations.

Calendar Date	WDS	Filter	$\theta$ Obs	$\sigma(\theta)$	$\rho$ Obs	$\sigma(\rho)$	Exposure	# Frames	# Sets
Bessel Date	Discovery		(deg)	(deg)	(arc-sec)	(arc-sec)	(sec)		
2020-10-20	22280+5742	g'	208.30	0.84	2.035	0.021	0.050	1000	5
2020.805	KR 60AB	r'	207.73	0.15	2.054	0.004	0.060	1000	5
		i'	207.84	0.21	2.039	0.029	0.080	1000	4
		z'	207.95	0.03	2.044	0.019	0.120	1000	5
Overall Average ==>			208.00		2.043				
Overall Std Deviation ==>			0.49		0.020				
2020-10-31	22280+5742	g'	209.03	2.28	2.067	0.073	0.060	1000	3
2020.835	KR 60AB	r'	207.53	0.54	2.089	0.012	0.080	1000	3
		i'	206.69	0.12	2.094	0.010	0.080	1000	3
		z'	206.87	0.25	2.070	0.015	0.150	1000	3
Overall Average ==>			207.53		2.080				
Overall Std Deviation ==>			1.39		0.035				
2020-12-04	22280+5742	g'	206.08	0.47	2.046	0.045	0.060	300	3
2020.928	KR 60AB	r'	206.32	0.48	2.055	0.019	0.060	300	3
		i'	206.81	0.03	2.056	0.010	0.080	300	3
		z'	206.59	0.08	2.052	0.013	0.150	300	3
Overall Average ==>			206.45		2.052				
Overall Std Deviation ==>			0.41		0.022				
2020-11-28	23050+3322	g'	166.29	0.15	2.676	0.004	0.020	1000	6
2020.912	STF 2974	r'	166.16	0.06	2.686	0.003	0.030	1000	6
		i'	166.14	0.07	2.687	0.004	0.080	1000	6
		z'	166.47	0.14	2.683	0.004	0.300	1000	6
Overall Average ==>			166.27		2.683				
Overall Std Deviation ==>			0.17		0.006				
2020-12-15	00014+3937	g'	163.17	1.03	1.354	0.006	0.030	500	4
2020.958	HLD 60	r'	164.64	0.79	1.351	0.008	0.040	500	4
		i'	165.69	1.05	1.352	0.030	0.080	500	4
		z'	165.64	0.54	1.359	0.008	0.300	500	2
Overall Average ==>			164.66		1.353				
Overall Std Deviation ==>			1.35		0.016				
2021-01-15	04301+1538	g'	14.58	0.74	1.509	0.012	0.020	1000	4
2021.041	STF 554	r'	15.35	0.55	1.524	0.025	0.030	1000	5
		i'	16.74	1.24	1.507	0.040	0.060	1000	5
		z'	14.65	1.00	1.468	0.023	0.100	1000	3
Overall Average ==>			15.45		1.505				
Overall Std Deviation ==>			1.23		0.032				
2021-02-06	04301+1538	g'	14.67	0.14	1.466	0.010	0.030	500	4
2021.101	STF 554	r'	14.49	0.33	1.436	0.023	0.030	500	4
		i'	15.54	0.96	1.416	0.026	0.060	500	4
		z'	14.56	1.25	1.424	0.036	0.200	500	4
Overall Average ==>			14.82		1.435				
Overall Std Deviation ==>			0.85		0.030				

## 10. Conclusions

Although this was just an exploration of possibilities, we were able to draw eight tentative conclusions:

- Speckle BSA processing in STB gives repeatable flux proportions.
- The primary sources of error are probably shot noise from low signal in some filters (the combination of filter, camera QE and star color), and high or rapidly varying extinction.
- Long exposures give reasonable photometric calibration, using the binary star itself as a secondary standard.
- Many of the binaries with known spectral type for both components are relatively bright, making it difficult to find  $g' r' i' z'$  magnitudes from photometric surveys. APASS10 has the most consistent Sloan data for brighter stars. Gaia ATLAS transformations may also be used.
- The speckle photometry method provided reasonably good estimates of component Spectral Types, for the range of A F G K M normal dwarf stars observed. However, because the secondary stars were *always* estimated to be *later* than WDS, there may be a systematic error in applying the combined light from surveys (typically dominated by the primary star) as a calibration factor to both components.
- Photometric nights provided good results with small scatter, but marginal nights (high humidity or high extinction) produced more scatter, even when employing frequent long (calibration) exposures.
- A change in the sequence of observation should reduce photometric scatter, by observing half (5) of the long exposures before the speckle exposures, and then the other half after the speckle frames.
- It may be possible to eliminate the long calibration exposures completely, by processing the speckle exposures in a different way, in addition to BSA: stacking all the hundreds of short speckle exposures to create a single long exposure with an equivalent unresolved atmospheric seeing disk. This technique would require rough centroiding to account for telescope tracking drift, but it could be explored in the future.

## Acknowledgements

This research has made use of the Washington Double Star Catalog and 6<sup>th</sup> Orbit Catalog, maintained at the U.S. Naval Observatory, the AAVSO Photometric All-Sky Survey (APASS) funded by the Robert Martin Ayers Sciences Fund and NSF AST-1412587, and results from the European Space Agency's Gaia mission. Gaia DR2 data was processed by the Gaia Data Processing and Analysis Consortium (DPAC), funded by national institutions participating in the Gaia Multi-Lateral Agreement (MLA). The authors appreciate the Sidereal Technology control system electronics and comprehensive SiTech ZWOCam user interface software enabling remote observation provided by Dan Gray.

## References

- Altunin, I., Wasson, R., Genet, R., "Observations of Potential Gaia DR2 Red Dwarf Binary Stars in the Solar Neighborhood – II," *JDSO*, **16-5**, 470, November 2020.
- AAVSO web site, 2020. <https://www.aavso.org/download-apass-data>
- Caputo, R., Marchetti, C., Teagarden, J., Armstrong, J.D., Wiese, C., Tock, K., Genet, R., Harshaw, R., Wasson, R., Freed, R., "First Remote Student Speckle Interferometry Double Star Observations on the InStAR Student Robotic Telescope Network," *JDSO*, **16-5**, 458, November 2020.
- Carrasco, Josep M., Gaia web site, Section 5.3.7 "Photometric relationships with other photometric systems," <https://gea.esac.esa.int>, taken from S. Alam, F. D. Albareti, C. Allende Prieto, F. Anders, S. F. Anderson, T. Anderton, B. H. Andrews, E. Armengaud, É. Aubourg, S. Bailey and et al., 2015. "The 11th and 12th Data Releases of the Sloan Digital Sky Survey: Final Data from SDSS-III." *ApJS*, **219**, pp. 12.

- Davidson, James W. Jr., Brian J. Baptista, Elliott P. Horch, Otto Franz, and William F. van Altena, 2009. "A PHOTOMETRIC ANALYSIS OF SEVENTEEN BINARY STARS USING SPECKLE IMAGING," *The Astronomical Journal*, **138**, pp 1354–1364, November 2009.
- Gray, Dan, et al., 2020. Personal communications.
- Harshaw, R., Rowe, D., Genet, R., 2017. "The Speckle Toolbox: A Powerful Data Reduction Tool for CCD Astrometry," *Journal of Double Star Observations*, **13-1**, 52, January 2017.
- Horch, Elliott P., Zoran Ninkov, Otto G. Franz, 2001. "CCD SPECKLE OBSERVATIONS OF BINARY STARS FROM THE SOUTHERN HEMISPHERE - III. DIFFERENTIAL PHOTOMETRY," *The Astronomical Journal*, **121**: 1583, March 2001.
- Horch, Elliott P., Meyer, Reed D., van Altena, William F., 2004. "SPECKLE OBSERVATIONS OF BINARY STARS WITH THE WIYN TELESCOPE - IV. DIFFERENTIAL PHOTOMETRY," *The Astronomical Journal*, **127**, 1727–1735, March 2004.
- Horch, Elliott P., 2006. "THE STATUS OF SPECKLE IMAGING IN BINARY STAR RESEARCH," *RevMexAA (Serie de Conferencias)*, **25**, 79–82, 2006.
- Johnson, H.L. and Morgan W.W., 1953. "FUNDAMENTAL STELLAR PHOTOMETRY FOR STANDARDS OF SPECTRAL TYPE ON THE REVISED SYSTEM OF THE YERKES SPECTRAL ATLAS," *Astrophysical Journal*, **117**, pp 313–352, 1953.
- Mamajek, E.E., 2019. University of Rochester website of Eric Mamajek: [http://www.pas.rochester.edu/~emamajek/EEM\\_dwarf\\_UBVIJHK\\_colors\\_Teff.txt](http://www.pas.rochester.edu/~emamajek/EEM_dwarf_UBVIJHK_colors_Teff.txt), Version 2019.3.22.
- Marchetti, Calla, Ryan Caputo, and Russell Genet, 2020. "The Fairborn Institute Robotic Observatory: First Observations," *JDSO*, **16-5**, 444, November 2020.
- Marchetti, C., Duan, X. and Nordenholz, S., 2021. "Remote Speckle Interferometry of Undiscovered Double Stars," *JDSO*, **17-1**, 81, January 2021.
- McAlister, Harold A., 1985. "High Angular Resolution Measurements of Stellar Properties," *Annual Review of Astronomy & Astrophysics*, **23**, 59-87, 1985.
- Pecaut, M.J. & Mamajek, E.E., 2013. "INTRINSIC COLORS, TEMPERATURES, AND BOLOMETRIC CORRECTIONS OF PRE-MAIN-SEQUENCE STARS," *ApJS*, **208**, 9, Sept 2013.
- Rogers, Christopher T., Ron Canterna, J. Allyn Smith, Michael J. Pierce, and Douglas L. Tucker, 2006. "IMPROVED u' g' r' i' z' TO U B V Rc Ic TRANSFORMATION EQUATIONS FOR MAIN-SEQUENCE STARS," *The Astronomical Journal*, **132**, pp 989-993, September 2006.
- Rowe, D., and Genet, R., 2015. "User's Guide to PS3 Speckle Interferometry Reduction Program," *Journal of Double Star Observations*, **11-1S**, 266, September 2015.
- Rowe, D., 2017. "Guide to Using WDS1.2 Search Tool for the WDS Catalog," private communication, 2017.
- Rowe, D., 2018. "Guide to GDS1.00 Gaia DR2 Double Star Catalog," private communication, July 17, 2018.
- Rowe, D., 2020. "Speckle ToolBox 1.14 Bispectrum Data Reduction Tools," private communication presentation to Stanford On-Line High School students, June 26, 2020.
- Tonry, J. L., L. Denneau, H. Flewelling, A. N. Heinze1, C. A. Onken, S. J. Smartt, B. Stalder, H. J. Weiland, C. Wolf, 2018. "The ATLAS All-Sky Stellar Reference Catalog," *The Astrophysical Journal*, **867**, 105, November 10, 2018.
- Wasson, R., Rowe, D., Genet, R., 2020. "Observation of Gaia (DR2) Red and White Dwarf Binary Stars in the Solar Neighborhood," *Journal of Double Star Observations*, **16-3**, 208, June 2020.